

Pix2HDR - A pixel-wise acquisition and deep learning-based synthesis approach for high-speed HDR videos

Caixin Wang*, Jie Zhang*, Matthew A. Wilson, Ralph Etienne-Cummings

Abstract—Accurately capturing dynamic scenes with wide-ranging motion and light intensity is crucial for many vision applications. However, acquiring high-speed high dynamic range (HDR) video is challenging because the camera’s frame rate restricts its dynamic range. Existing methods sacrifice speed to acquire multi-exposure frames. Yet, misaligned motion in these frames can still pose complications for HDR fusion algorithms, resulting in artifacts. Instead of frame-based exposures, we sample the videos using individual pixels at varying exposures and phase offsets. Implemented on a pixel-wise programmable image sensor, our sampling pattern simultaneously captures fast motion at a high dynamic range. We then transform pixel-wise outputs into an HDR video using end-to-end learned weights from deep neural networks, achieving high spatiotemporal resolution with minimized motion blurring. We demonstrate aliasing-free HDR video acquisition at 1000 FPS, resolving fast motion under low-light conditions and against bright backgrounds — both challenging conditions for conventional cameras. By combining the versatility of pixel-wise sampling patterns with the strength of deep neural networks at decoding complex scenes, our method greatly enhances the vision system’s adaptability and performance in dynamic conditions.

Index Terms—High-dynamic-range video, high-speed imaging, CMOS image sensors, programmable sensors, deep learning, convolutional neural networks.

I. INTRODUCTION

DIGITAL cameras have become integral to many vision applications, including videography, smart devices, autonomous vehicles, and scientific research. The camera’s performance directly impacts these systems, and failure to capture crucial video features can have critical consequences. However, conventional cameras have limited dynamic range and temporal resolution at a fixed frame rate. They struggle to capture scenes with a large range of motion and intensities: fast events are susceptible to aliasing and blurring, high-intensity events cause overexposure, and low-light regions suffer from a low signal-to-noise ratio (SNR).

Extending the dynamic range for high-speed videos is fundamentally challenging, given the conventional camera’s inability to accommodate multiple exposures at each video

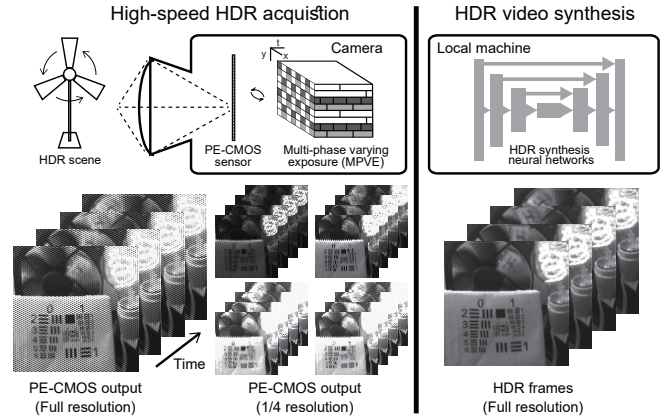


Fig. 1. The overview of the Pix2HDR acquisition / synthesis. Pix2HDR acquires the HDR scene using the multi-phase varying exposure (MPVE) pixel-wise sampling pattern, implemented on a CMOS image sensor (PE-CMOS). MPVE configures pixels into different exposures, speeds, and phase offsets to enhance temporal resolution and dynamic range. Pix2HDR synthesizes a high spatiotemporal HDR video from pixel-wise outputs using weights obtained through a deep neural network through end-to-end training, achieving high spatiotemporal resolution with minimized motion blurring.

frame. While multi-camera systems are commonly employed to boost dynamic range, they do so at the expense of large size, higher power consumption and complexity [1]–[3]. Alternatively, computational techniques can merge time-interleaved frames acquired from a single camera at both short and long exposures to extend the dynamic range [4], [5]. But its performance heavily relies on motion alignment accuracy and may introduce ghosting artifacts.

Recent innovations enable computational imaging sensors and systems to control exposure at the pixel level [6]–[15]. This allows them to capture local high-light areas in an HDR scene with adjacent pixels configured in varying exposure durations. While the pixel-wise imaging configuration significantly simplifies cross-frame motion alignment, it comes at the expense of reduced spatial resolution [7]. Furthermore, the temporal resolution of these systems is limited by the longest-exposing pixels [6], [11], [12]. While computational methods can recover video motion faster than the frame rate using Compressed Sensing principles, the reconstruction performance heavily depends on scene sparsity [6], [9], [11], [12], [16].

We present a pixel-wise imaging approach (Pix2HDR) for sampling HDR scenes at high-speed. Pix2HDR first acquires

C. Wang and R. Etienne-Cummings are with the Department of Electrical and Computer Engineering, The Johns Hopkins University, Baltimore, MD, USA

J. Zhang and M.A. Wilson are with the Picower Institute for Learning and Memory and the Department of Brain and Cognitive Sciences, Massachusetts Institute of Technology, Cambridge, MA, USA

* C. Wang and J. Zhang contributed equally

the scene using a multi-phase varying exposure pixel-wise exposure pattern (MPVE) (**Fig. 1**). By using multiple pixels at different exposure durations and phase offsets, MPVE guarantees that each small pixel patch captures high-temporal resolution scene details with an extended dynamic range. Pix2HDR then transforms pixel-wise outputs into high-speed HDR videos using a deep neural network (LDR-HDR network) (**Fig. 1**), leveraging learned weights to achieve high spatiotemporal resolution and dynamic range while eliminating aliasing and motion blur.

The rest of the paper is organized as follows: Section II provides a short summary of previous works. Section III offers a brief overview of our system, and in Section IV, we outline an optimized pixel-wise strategy for capturing HDR videos. Section V then delves into the specifics of Pix2HDR’s architecture for synthesizing high-speed HDR videos from pixel-wise outputs. For results in Section VI, we first evaluate our method’s performance against other works using publicly available datasets. We then capture HDR scenes using our method to assess its spatial resolution, temporal resolution, dynamic range, motion deblurring performance, and the capability to detect object motion under low-light conditions and against bright backgrounds. We conclude in Section VII by discussing its applications, greater impact, system limitations, and future work.

II. PREVIOUS WORK ON HDR IMAGING

1) *Acquiring and merging multiple frames of varying exposure*: Learning-based or classic tone-mapping methods can merge time-synchronized low dynamic range (LDR) frames captured at different exposures into a single HDR frame [17]–[28]. However, the performance of these methods depends on additional alignment techniques to rectify differences between frames due to motion, overexposure, and occlusions. Failure to synchronize the LDR frames results in ghosting artifacts in the merged HDR frame.

Obtaining time-aligned frames can also be challenging and often requires using multiple cameras. These setups either split incoming light using beam splitters among different cameras [3], [29], [30], or employing an array of cameras, each with its independent optical path [1], [2], [31]. Multi-camera systems add significant complexity, bulkiness, and increased power consumption. Moreover, dividing the incoming light among multiple detectors degrades the overall SNR. Additionally, camera arrays demand parallax correction to align cameras’ FOV, which leaves room for artifacts and errors.

2) *HDR imaging through pixel-wise exposure modulation*: Pixel-wise exposure modulation allows precise control of each pixel’s exposure duration. Given natural scenes’ inherent high spatial correlation, local pixels, set with distinct exposures, can capture the scene at varying dynamic ranges. This method simplifies the alignment between multiple exposure pixels and allows HDR reconstruction using simple spatial filtering (or learning-based methods) but at the cost of lower spatial resolution [6]–[10], [13], [32].

Previously implemented sensors with pixel-wise exposure control have several key disadvantages: exposure control circuits at the pixel level occupy valuable detector areas and

reduce the photodiode fill factor [6], [33]. This degrades the pixel sensitivity compared to a conventional CMOS image sensor. Furthermore, previous pixel-wise exposure sensors have slow frame rates (~ 30 FPS), constrained by the longest pixel exposure duration [6]–[8], [32], [34], [35]. This leads to pixels with shorter exposures operating at the same sampling rate as those with longer exposures and limits the sensor’s ability to perform high-speed imaging.

III. OVERVIEW

The Pix2HDR consists of an acquisition system and a synthesis method (**Fig. 1**). The acquisition system is a camera built with the pixel-wise programmable exposure (PE-CMOS) image sensor [36]. Individual pixels in PE-CMOS can be separately exposed. This feature allows for different exposure durations and phases at each pixel, making it possible to coordinate their configurations to optimize the temporal resolution and dynamic range during high-speed imaging. PE-CMOS features an efficient pixel design and achieves a 75% photodiode fill factor with a $10\ \mu\text{m}$ pixel pitch. The PE-CMOS has comparable low-light performance to state-of-the-art low-noise CMOS sensors without pixel-wise exposure control [36].

Using the PE-CMOS sensor, we implemented the MPVE sampling pattern optimized for high-speed HDR imaging. In MPVE, neighboring pixels have variable exposure, sampling rate, and phase offsets (**Fig. 1**). As we will demonstrate in Section IV, varying pixel-wise exposure expands the dynamic range and prevents motion blur. Relative phase offsets in adjacent pixels enhance the acquisition’s temporal resolution without increasing pixel sampling speed. We will show that with a 250 Hz pixel sampling rate, the Pix2HDR method can sample the scene with a 1000 Hz temporal resolution.

The Pix2HDR video synthesis algorithm employs deep neural networks to determine the optimal weights for converting the sensor’s pixel outputs into high-speed HDR video. The deep learning-based method efficiently addresses the conflicting demands of high spatiotemporal resolution and dynamic range while preventing aliasing and motion blur. As described in Section V, the Pix2HDR synthesis networks, implemented on an Nvidia RTX3080, have achieved an average frame inference time of 2.5 ms and support a 400 FPS real-time HDR video synthesis.

IV. MULTI-PHASE VARYING EXPOSURE (MPVE) PIXEL-WISE SAMPLING CONFIGURATION

We proposed the MPVE pixel-wise sampling configuration to maximize temporal resolution, SNR (for fast transient events and static scenes) and dynamic range at sampling HDR scenes. Here we discuss each consideration and derive the MPVE sampling pattern for HDR video acquisition.

A. Eliminating temporal aliasing with pixel-wise phase offset

The camera’s temporal resolution is an essential consideration for high-speed imaging. The selection of pixel exposure, T_E , establishes the pixel’s sampling rate to $1/T_E$, along with its Nyquist bandwidth at $1/(2T_E)$. For a conventional camera, where pixels are either all simultaneously integrated (global

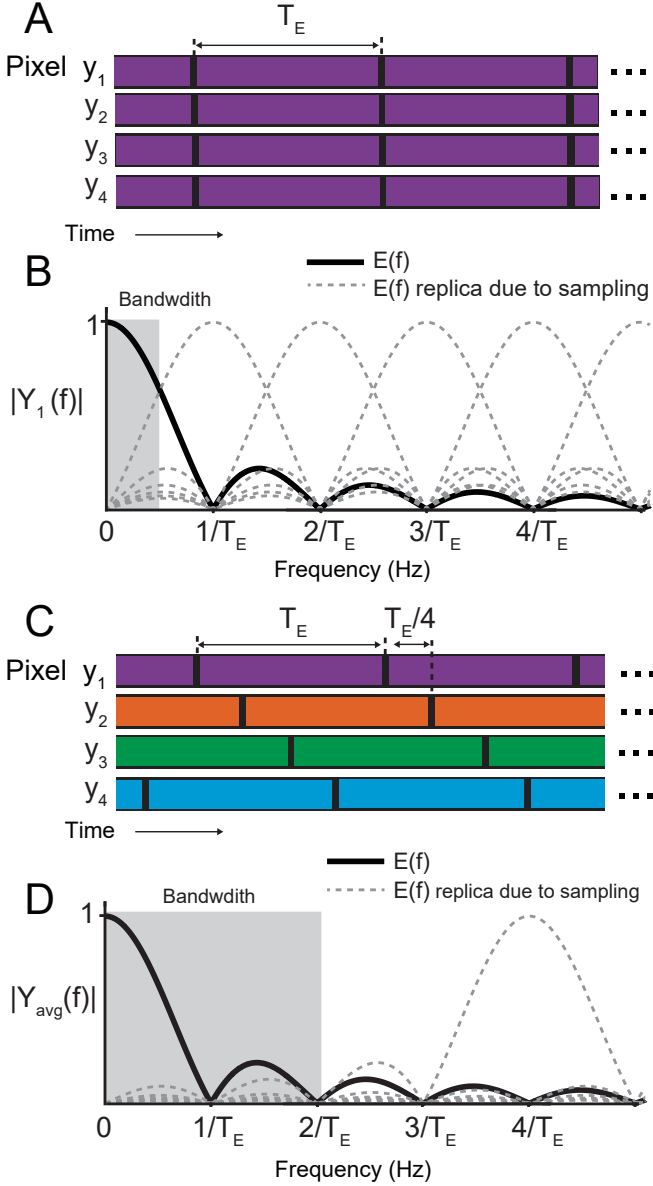


Fig. 2. Multi-phase sampling enhances the temporal resolution without increasing sampling speed. **A**. Conventional camera samples all the pixels (y_1, \dots, y_4) concurrently (global shutter) or in fast line sequences (rolling shutter) with pixel exposure of T_E and sampling rate at $1/T_E$. **B**. Frequency spectrum of the averaged pixel value, y_{avg} . Its Nyquist bandwidth is limited to $1/(2T_E)$ and suffers from a significant amount of temporal aliasing. **C**. In multi-phase sampling, pixels of exposure T_E are phase-offsetted in multiples of $T_E/4$. **D**. Without increasing the sampling rate, multi-phase exposures extend the y_{avg} bandwidth by four times to $2/T_E$ and mitigate temporal aliasing by pushing the replica spectra to higher frequencies.

shutter) or sequentially in rows (rolling shutter), the choice of T_E also limits the temporal resolution of the camera (Fig. 2A). We can increase the temporal resolution by shortening T_E . But it comes at the cost of lower SNR and higher sampling speed and higher power consumption.

While we cannot increase the temporal resolution of a single pixel without reducing T_E , we could exploit the phase relationship between multiple pixels to enhance the sensor's temporal resolution. This approach is viable due to the inherent spatial correlations of natural scenes, where closely situated

pixels capture closely related activities. To illustrate (Fig. 2), we assume a light impulse, $\delta(t)$, is simultaneously sampled by 4 adjacent pixels, $y_1(n), \dots, y_4(n)$, each with an exposure function $e(t)$. The single pixel output $y_1(t)$ is:

$$y_1(t) = e(t) * \delta(t), \quad e(t) = \begin{cases} 1, & 0 \leq t \leq T_E, \\ 0, & \text{otherwise,} \end{cases} \quad (1)$$

$y_1(t)$ is then sampled by an ADC at a period of T_E , the discretized version, $y_1[n]$ is:

$$y[n] = y(nT_E), \quad (2)$$

with frequency spectrum:

$$Y_1(f) = \frac{1}{T_E} \sum_{n=-\infty}^{\infty} E(f - \frac{n}{T_E}), \quad (3)$$

where $E(f - n/T_E)$ are the replicas of the exposure function's spectrum resulting from sampling. We can plot $Y_1(f)$ to see that the majority of the frequency spectrum is aliased, resulting in signal distortion (Fig. 2B).

By relying on the phase difference between neighboring pixels, we can eliminate the aliasing effect without increasing each pixel's sampling speed. To achieve this, relative to the phase of pixel 1, we can introduce phase shifts of $T_E/4, T_E/2, (3T_E)/4$ to pixel 2, 3, and 4 respectively (Fig. 2C). These pixels' spectrum, $Y_k(f)$, becomes:

$$Y_k(f) = \frac{1}{T_E} \sum_{n=-\infty}^{\infty} E(f - \frac{n}{T_E}) e^{-j2\pi \frac{n(k-1)}{4}}, \quad (4)$$

where $k \in \{1, 2, 3, 4\}$. If we average these four pixels, the resulting spectrum becomes:

$$Y_{avg}(f) = \frac{1}{4} \sum_{k=1}^4 Y_k(f) = \frac{1}{4T_E} \sum_{n=-\infty}^{\infty} E(f - \frac{n}{T_E}) \sum_{k=1}^4 e^{-j2\pi \frac{n(k-1)}{4}}, \quad (5)$$

since $Y_{avg}(f) = 0$ when n is not a multiple of 4, the above equation can be rewritten as:

$$Y_{avg}(f) = \frac{1}{4T_E} \sum_{n=-\infty}^{\infty} E(f - \frac{4n}{T_E}), \quad (6)$$

which spaces the frequency replicas of $E(f)$ away from each other and avoids aliasing (Fig. 2D). The average spectrum of phase shifted pixels increases the Nyquist bandwidth of individual pixels by four times, without increasing in per-pixel sampling rate. From a time-domain viewpoint, the combined phase-shifted pixel outputs are equivalent to the sampling of the impulse signal, $\delta(t)$, at a higher rate of $4/T_E$. We will demonstrate this using an experiment in Section VI (Fig. 11)

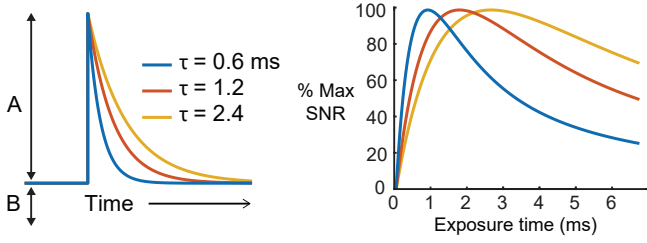


Fig. 3. Exposure duration determines pixel SNR at sampling high-speed events. To illustrate: **Left**. Transient events of amplitude A with baseline intensity B , and different falling time constants (τ) of 0.6, 1.2 and 2.4 ms. **Right**. Pixel SNR with respect to the exposure time, T_E , for the signals on the left. Each curve is normalized with the maximum SNR set to 100%. The SNR increases with longer exposure time but drops as extra integration time adds more shot noise than signal power.

B. Maximizing SNR for high-speed signals

Maximizing the SNR for detecting ultra-fast events is another important consideration for the pixel sampling pattern. Fast events can result from various phenomena, such as the fast fluorescent intensity change in biological tissues (neurons, cardiac cells, etc.) and the rapid movement of small objects, whose signals appear as pulsed events at individual pixels. The optimal duration of exposure that maximizes the SNR for detecting these events depends on the temporal characteristics of the signal. The SNR may be compromised if pixels are sampled with an inappropriate exposure time: A short exposure time is inadequate for pixel to integrate the signal, while an excessively long exposure time increases shot noise without increasing signal power, resulting in SNR degradation.

We can demonstrate this by deriving an expression for a pixel's SNR. Let $v(t)$ represent a fast transient signal at a particular pixel. This could result from the movement of an ultra-fast object or the fast change of light intensity of a stationary object. For simplicity, $v(t)$ is denoted as a signal with an instantaneous rise time and a fall time modeled by an exponential function with time constant, τ , amplitude A , and baseline intensity B (**Fig. 3**):

$$v(t) = \begin{cases} B, & \text{when } t < 0, \\ B + Ae^{-t/\tau}, & \text{when } t \geq 0. \end{cases} \quad (7)$$

Using Eq.1, the pixel output $y(t)$ is obtained as the convolution result between $v(t)$ and the exposure $e(t)$. The discrete samples, $y[n]$, of the resulting output are written as:

$$y[n] = y(nT_E) + \sigma[n], \quad (8)$$

where $\sigma[n]$ is the noise containing both shot noise and circuit read noise. The shot noise is described by a Poisson distribution with a rate factor λ equal to the signal at the pixel. As such, the noise power is expressed as:

$$N_{\text{shot}} = y[n] + B \cdot T_E, \quad (9)$$

If we assume the pixel is operating in a shot noise-limited region, where the read noise is negligible (i.e. $B \gg N_{\text{read}}$). The SNR can be expressed as:

$$\text{SNR} = \frac{S}{N_{\text{shot}}} = \frac{\max\{y\}^2}{\max\{y\} + B \cdot T_E}. \quad (10)$$

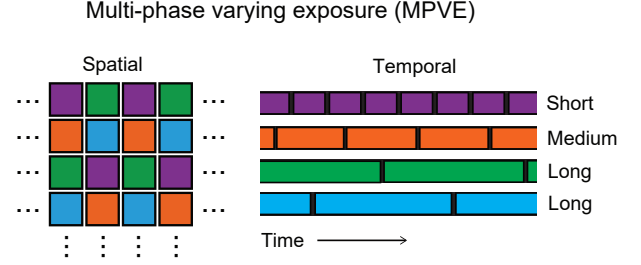


Fig. 4. MPVE sampling pattern uses varying exposures (short, medium, and long) at different phase offsets to maximize SNR for signals of different temporal characteristics.

We plotted the SNR with respect to T_E for signals of different time constants (**Fig. 3**). The SNR curves exhibit a concave pattern in relation to T_E : SNR first grows as the increase in T_E allows more signal energy to be integrated into the pixel. However, once a peak value is reached, further increase of T_E no longer results in additional energy integration but raises the shot noise power due to the baseline intensity, B .

The relationship of SNR with T_E indicates that a continuous exposure function of appropriate duration is the key to maximizing SNR. To improve the SNR of signals encompassing a range of frequencies, we can configure adjacent pixels to have different exposure durations (**Fig. 4**). This leads to the Multi-Phase Varying Exposure (MPVE) pixel-wise sampling pattern. Every 2×2 patches are arranged to have a short ($T_E/2$), medium (T_E) and long exposure ($2T_E$) arranged with relative phase offset of $T_E/4$, reaching the overall temporal resolution of $T_E/4$.

We can qualitatively illustrate the MPVE's advantages over other patterns at sampling a signal with diverse temporal characteristics (**Fig. 5A**). The signal, common to four pixels (y_1, \dots, y_4), comprises a faint, slowly fluctuating baseline with two rapid burst events occurring 4 ms apart. MPVE's phase-shifted pixel arrangement ensures that fast events' timing can be unambiguously acquired (**Fig. 5A**). In addition, short exposures are used to maximize the SNR of the burst events. At the same time, the medium and long exposure at y_2, y_3 and y_4 enhances the SNR of the weak baseline signal.

In contrast to MPVE, the time-interleaved long-short exposure method introduces aliasing in frames when burst events coincide with a long exposure periods (**Fig. 5B**). The long exposure also limits the maximum frame rate. Similarly, in pixel-wise coded exposure, the random arrangement of exposure times can create ambiguity when trying to resolve the timing of fast events: the pixel outputs will be identical if a spike occur at the two aliased frames, causing ambiguity (**Fig. 5C**). Furthermore, this approach results in lower pixel SNR because photons are not sampled during exposure off-times.

C. Minimizing blurring and extending the dynamic range

The MPVE naturally extend the sampled dynamic range within a 2×2 pixel patch, as pixels acquire the scene irradiance at different exposures. In addition, The varying pixel exposures also suppress blurring that would have occurred if all pixels

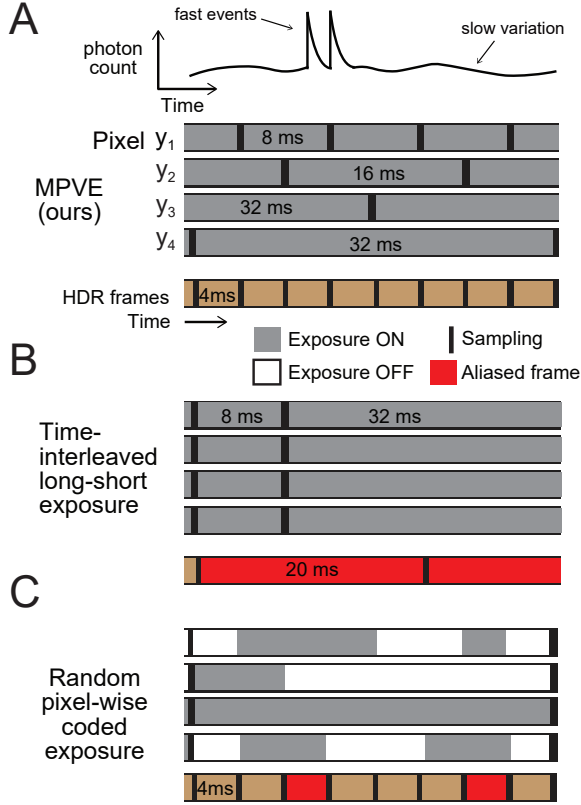


Fig. 5. Temporal comparison of MPVE vs other sampling patterns. **A.** Sampling a signal that consists of a slow variation with two closely spaced fast events, the MPVE guarantees aliasing-free sampling at high time resolution. Long pixel exposure also increases the SNR of the slow variations and expands the dynamic range. **B.** Sampling the same signal using time-interleaved long-short exposure will introduce aliasing, unable to resolve the timing of these two events. **C.** Multiple-on coded exposure pattern distributed randomly also creates aliasing: events appearing at either of the red colored frames generate the same reading at all pixel outputs, creating ambiguity in the events’ timing.

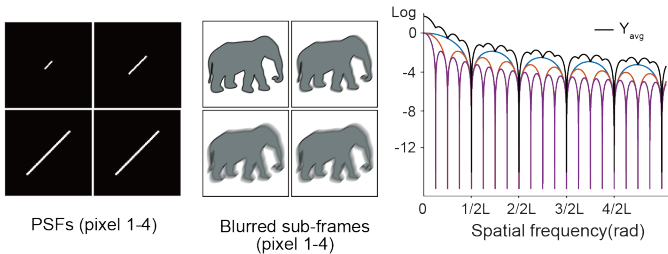


Fig. 6. PSF kernels of the MPVE exposure pattern. The same motion translates to PSF length $2L$ to $8L$ for at pixel y_1 to y_4 , depending on their exposure. The corresponding spectra are sinc functions with zeros at multiples of $1/2L$, $1/4L$, $1/8L$, causing unrecoverable blurring effects. The spectrum of MPVE output, Y_{avg} , eliminates zeros except at $1/2L$, achieving a deblurring goal of which means the blurring effect of ideal recovered frame keeps at $2L$.

were exposed for the same duration. To illustrate, a motion across the FOV translates to point spread function (PSF) of length $2L$ to $8L$ at pixel y_1 to y_4 , depending on their exposure length (Fig. 6). These PSF’s spectra contain zeros that cause unrecoverable blurring effects [37]. The PSF of the averaged pixel values in MPVE, y_{avg} , can eliminate the zeros except at

locations multiples of $1/2L$, reaching a deblurring resolution of $2L$. Incorporating non-integer multiples of pixel exposures can improve deblurring performance. However, its implementation might require adopting an alternative spatiotemporal pixel configuration, with distinct trade-offs in anti-aliasing and dynamic range.

V. LDR-HDR NETWORKS FOR SYNTHESIZING HDR VIDEOS FROM PIXEL-WISE OUTPUTS.

With MPVE, each small pixel patch of PE-CMOS captures high-temporal resolution scene details with an extended dynamic range. The proposed video synthesis algorithm aims to convert pixel outputs into a high-speed HDR video, achieving high spatiotemporal resolution and dynamic range while eliminating aliasing and motion blur. Conventional linear models, which derive each pixel value through a linear combination of its neighboring pixels, often fail to meet all specifications simultaneously. Instead, we leverage a deep learning approach to find the optimal weights for transforming pixel-wise outputs into high spatiotemporal resolution HDR video.

Our proposed LDR-HDR architecture consists of a pair of 3D CNN networks: LDR-net and HDR-net. LDR-net handles spatiotemporal upsampling/interpolation by transforming PE-CMOS outputs into three videos, $[\hat{y}_{low}, \hat{y}_{mid}, \hat{y}_{high}]$ (Fig. 7). These videos of lower dynamic range (LDR), with a spatial resolution of $N_c \times N_r$ and a temporal resolution of N_t , render the scenes at low, medium, and high irradiance levels. Meanwhile, HDR-net is responsible for HDR fusion, combining high-speed, high-resolution, low dynamic range video stacks into a single tone-mapped HDR video (Fig. 7). Here we discuss the details of training data generation and the architecture of LDR-HDR network.

A. Training data generation: transforming ground truth HDR video to pixel outputs

We generate training data using public HDR video datasets (hdm-hdr-2014) [30]. This process is summarized in Fig. 7 and expanded into details in Fig. 8. Original HDR video cube, $\mathbf{p}_{orig} \in \mathbb{R}^{N_r \times N_c \times N_t}$, is first normalized by clipping the 1% intensity outliers to $p_{99\%}$, the 99% percentile of the intensity range:

$$\mathbf{p} = \text{clip}\left(\frac{\mathbf{p}_{orig}}{p_{99\%}}\right), \quad (11)$$

where, $\mathbf{p} \in \mathbb{R}^{N_r \times N_c \times N_t}$, is ground truth video and $\text{clip}(\cdot)$ operations set any pixel value that is outside the range $[0,1]$ to 1.

\mathbf{p} is then transformed into pixel measurements, $\mathbf{y}_{mea} \in \mathbb{R}^{N_r \times N_c \times N_t}$ through modulation with the exposure cube, \mathbf{e} :

$$\mathbf{y}_{mea} = \mathcal{R}(\mathbf{p} \odot \mathbf{e} + \mathbf{n}). \quad (12)$$

Here, the operator \odot represents the PE-CMOS camera’s operation of pixel integration and sampling (Fig. 7, 8). We ensure \mathbf{y}_{mea} has the same dimension as \mathbf{p} by up-sampling the resulting pixel values in time. A noise term, \mathbf{n} , consisting of read noise and shot components, is then added to the pixel values. $\mathcal{R}(\cdot)$ is the measured camera response function (CRF) that corrects for the camera’s non-linear response between

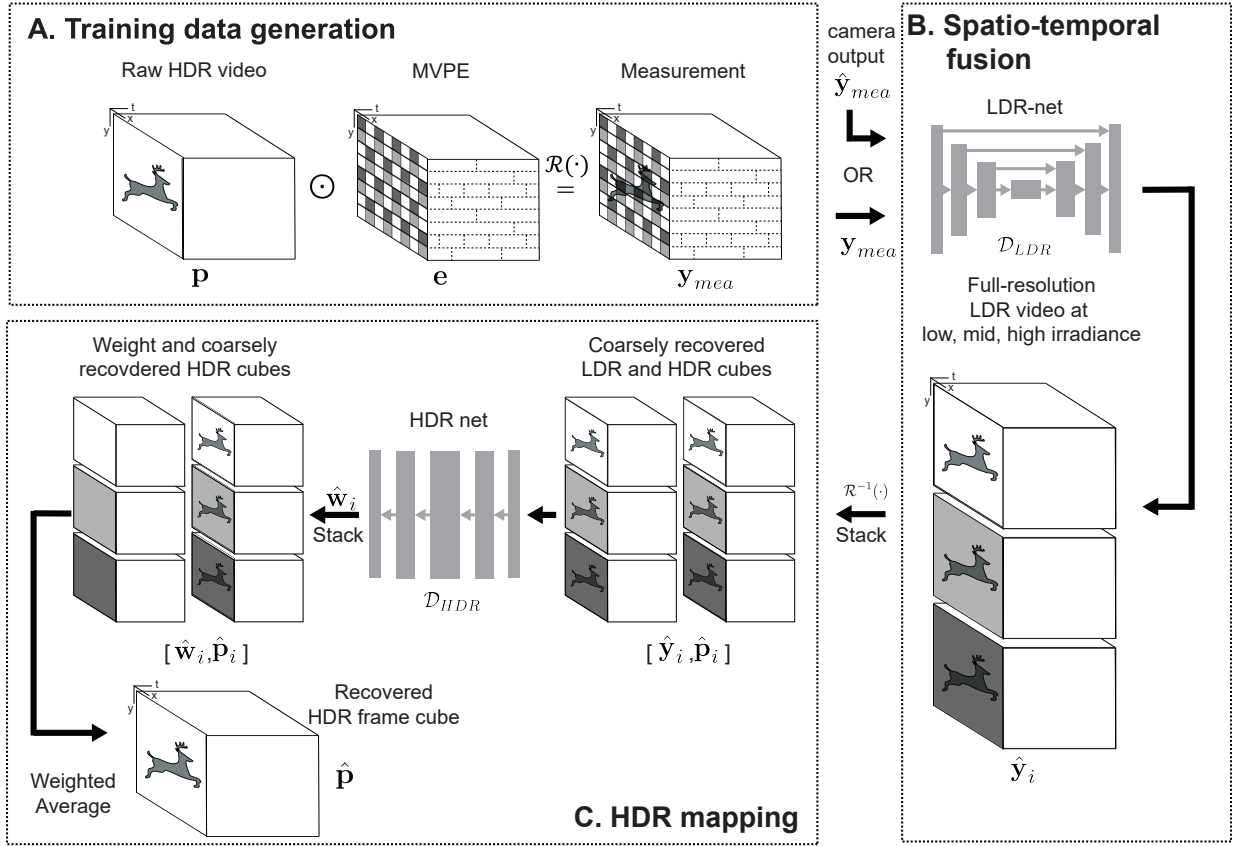


Fig. 7. LDR-HDR network for HDR video synthesis. **A.** Training data generation: The ground truth video, \mathbf{p} , are modulated by MVPE cube, \mathbf{e} , and then converted from irradiance value to camera outputs, \mathbf{y}_{mea} , through a camera response function (CRF), $\mathcal{R}(\cdot)$. **B.** Spatio-temporal fusion using LDR-net: \mathbf{y}_{mea} (for training) or $\hat{\mathbf{y}}_{mea}$ (for testing) are inputs into the LDR-net $\mathcal{D}_{LDR}(\cdot)$, which performs spatio-temporal up-sampling and renders three LDR video cubes $\hat{\mathbf{y}}_i$ at low, medium, and high exposure levels. **C.** HDR mapping using HDR-net: $\hat{\mathbf{y}}_i$ are first mapped to their corresponding irradiance, $\hat{\mathbf{p}}_i$, using the inverse CRF, $\mathcal{R}^{-1}(\cdot)$. Then $\hat{\mathbf{y}}_i$ and $\hat{\mathbf{p}}_i$ are inputs into the HDR-net $\mathcal{D}_{HDR}(\cdot)$ to obtain the weights $\hat{\mathbf{w}}_i$ to fuse $\hat{\mathbf{p}}_i$ into a single HDR video, $\hat{\mathbf{p}}$.

exposure and sampled pixel values (**Fig. 8**). Finally, \mathbf{y}_{mea} is quantized to a 10-bit resolution. The pairs of \mathbf{y}_{mea} and \mathbf{p} form the training data of the LDR-HDR networks (LDR-net and HDR-net).

B. LDR-net: Mapping pixel-wise outputs to high spatio-temporal resolution videos at different exposure levels

1) *LDR-net architecture:* The goal of the LDR-net, denoted as \mathcal{D}_{LDR} , is to transform pixel-wise outputs, $\hat{\mathbf{y}}_{mea}$, containing pixel outputs at different exposure, speed, and phase offsets, into three high-speed, high-spatial-resolution videos, $\hat{\mathbf{y}}_{low}, \hat{\mathbf{y}}_{mid}, \hat{\mathbf{y}}_{high}$, at low, medium and high exposure level. We adopted a 3D U-net architecture to accomplish this task: \mathcal{D}_{LDR} consists of an encoder module, a bottleneck module, and a decoder module. Three skip connections are attached between the encoder and decoder modules. Instead of using pooling layers, we adopt convolutional and transposed convolutional layers for down- and up-sample feature mapping.

The encoder module has three blocks: the first block consists of a $7 \times 7 \times 7$ convolutional layer followed by a leaky rectified linear unit (LeakyReLU) and a batch normalization layer. In the other two blocks, the convolutional layer is replaced by two $3 \times 3 \times 3$ convolutional layers. While the stride of the first

layer is 1, the stride length of the second layer rises to 2 to downsample the feature map size.

The bottleneck module contains 12 residual blocks, where each block has two $3 \times 3 \times 3$ convolutional layers, between which there are a LeakyReLU, a batch normalization layer, and a skip connection.

The decoder module contains three blocks, each of which contains a $4 \times 4 \times 4$ transposed convolutional layer with a stride equals to 2 and padding size equal to 1 (up-sampling layer), a $3 \times 3 \times 3$ convolutional layer, a LeakyReLU, and a batch normalization layer. The output video is non-linearized with a sigmoid function so that its range is between $[0,1]$. All operations are conducted in 4D tensors, and the input channel size is 1 (grayscale), and the output channel size is 3 (three LDR videos under low, mid, and high exposures).

2) *training:* \mathcal{D}_{LDR} learns the mapping for interpolating \mathbf{y}_{mea} to high spatiotemporal resolution LDR videos $[\hat{\mathbf{y}}_{low}, \hat{\mathbf{y}}_{mid}, \hat{\mathbf{y}}_{high}]$:

$$[\hat{\mathbf{y}}_{low}, \hat{\mathbf{y}}_{mid}, \hat{\mathbf{y}}_{high}] = \mathcal{D}_{LDR}(\mathbf{y}_{mea}). \quad (13)$$

To train the \mathcal{D}_{LDR} 's parameters, we first generate ground truth LDR videos from raw HDR video \mathbf{p} :

$$\mathbf{y}_{low} = \mathcal{R}(2\mathbf{p}), \quad \mathbf{y}_{mid} = \mathcal{R}(4\mathbf{p}), \quad \mathbf{y}_{high} = \mathcal{R}(8\mathbf{p}). \quad (14)$$

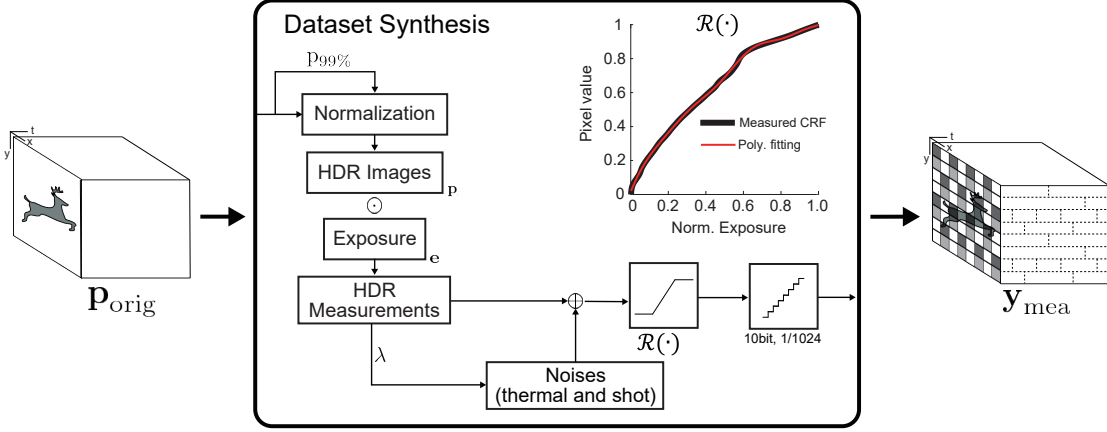


Fig. 8. Training data preparation. The training dataset, \mathbf{p}_{orig} , are firstly normalized with anchor irradiance value $p_{99\%}$ to get \mathbf{p} . We then obtain pixel output: $\mathbf{y}_{\text{mea}} = \mathcal{R}(\mathbf{p} \odot \mathbf{e} + \mathbf{n}_{\text{thermal}} + \mathbf{n}_{\text{shot}})$. $\mathcal{R}(\cdot)$ is the measured camera CRF function. \mathbf{n}_{shot} is the simulated shot noise with $\lambda = \mathbf{p} \odot \mathbf{e}$. $\mathbf{n}_{\text{thermal}}$ follows zero mean gaussian distribution with s.t.d set to the measured camera rms thermal noise. \mathbf{y}_{mea} is quantized to 10bits to reflect PE-CMOS outputs resolution.

The training process minimize the loss function $\mathcal{L}(\cdot)$ with the ADAM stochastic gradient-based optimization algorithm [38]:

$$\arg \min_{\mathcal{D}_{\text{LDR}}} \sum_i \mathcal{L}(\hat{\mathbf{y}}_i, \mathbf{y}_i), \quad (15)$$

where $i \in \{\text{low}, \text{mid}, \text{high}\}$ and $\mathcal{L}(\cdot)$ is a combination of three loss functions, defined as:

$$\mathcal{L} = \mathcal{L}_{\text{MSE}} + \mathcal{L}_{\text{perc}} + \mathcal{L}_{\text{SSIM}}. \quad (16)$$

3) *Loss function*: \mathcal{L}_{MSE} is the loss function minimize the mean square error between two images. $\mathcal{L}_{\text{perc}}$ is the perceptual loss of two images $\hat{\mathbf{I}}$ and \mathbf{I} defined as:

$$\mathcal{L}_{\text{perc}}(\hat{\mathbf{I}}, \mathbf{I}) = \mathcal{L}_1(\phi_k(\hat{\mathbf{I}}), \phi_k(\mathbf{I})), \quad (17)$$

where $\phi_k(\cdot)$ are features extracted from k^{th} layer of VGG16 network [39]. We use $k = 8$ for $\mathcal{L}_{\text{perc}}$.

$\mathcal{L}_{\text{SSIM}}$ is a loss function to maximize the structural similarity metric (SSIM) between two images [40], [41]. SSIM for image $\hat{\mathbf{I}}$ and \mathbf{I} is defined as:

$$\text{SSIM}(\hat{\mathbf{I}}, \mathbf{I}) = \frac{(2\mu_{\hat{\mathbf{I}}}\mu_{\mathbf{I}} + C_1)(2\sigma_{\hat{\mathbf{I}}\mathbf{I}} + C_2)}{(\mu_{\hat{\mathbf{I}}}^2 + \mu_{\mathbf{I}}^2 + C_1)(\sigma_{\hat{\mathbf{I}}}^2 + \sigma_{\mathbf{I}}^2 + C_2)}, \quad (18)$$

where $\mu_{\hat{\mathbf{I}}}$, $\sigma_{\hat{\mathbf{I}}}^2$, and $\sigma_{\hat{\mathbf{I}}\mathbf{I}}$ are the mean of $\hat{\mathbf{I}}$, the variance of $\hat{\mathbf{I}}$, and the covariance of $\hat{\mathbf{I}}$ and \mathbf{I} . C_1 and C_2 are constant values and we set them as $1e^{-4}$ and $9e^{-4}$ respectively. To evaluate SSIM, we use a sliding Gaussian window with a size equals to 11 to attain the mean $\text{SSIM}(\hat{\mathbf{I}}, \mathbf{I})$:

$$\text{MSSIM}(\hat{\mathbf{I}}, \mathbf{I}) = \frac{1}{M} \sum_{i=0}^M \text{SSIM}(\hat{\mathbf{I}}_i, \mathbf{I}_i). \quad (19)$$

The final $\mathcal{L}_{\text{SSIM}}$ is defined as:

$$\mathcal{L}_{\text{SSIM}}(\hat{\mathbf{I}}, \mathbf{I}) = 1 - \text{MSSIM}(\hat{\mathbf{I}}, \mathbf{I}). \quad (20)$$

C. *HDR-net: fusing multi-irradiance video into a single HDR video*

1) *HDR-net architecture*: The HDR-net, $\mathcal{D}_{\text{rmHDR}}(\cdot)$, is used to generate weight matrices $[\hat{\mathbf{w}}_{\text{low}}, \hat{\mathbf{w}}_{\text{mid}}, \hat{\mathbf{w}}_{\text{high}}]$ for fusing multiple LDR videos from \mathcal{D}_{LDR} into a single HDR video. We built $\mathcal{D}_{\text{HDR}}(\cdot)$ with 5 consecutive 3D CNN residual modules ($3 \times 3 \times 3$ convolutional layers inside). The HDR-net receives 6-channel 4D tensor (6 stacked video cubes) as the input and generates 3-channel 4D tensor (3 weight cubes) as the output.

2) *training*: $\mathcal{D}_{\text{HDR}}(\cdot)$ completes the following transformation:

$$\hat{\mathbf{w}}_i = \mathcal{D}_{\text{HDR}}(\hat{\mathbf{y}}_i, \hat{\mathbf{p}}_i), \quad i \in \{\text{low}, \text{mid}, \text{high}\}, \quad (21)$$

where $[\hat{\mathbf{p}}_{\text{low}}, \hat{\mathbf{p}}_{\text{mid}}, \hat{\mathbf{p}}_{\text{high}}]$ are derived from $\mathcal{D}_{\text{LDR}}(\cdot)$ outputs $[\hat{\mathbf{y}}_{\text{low}}, \hat{\mathbf{y}}_{\text{mid}}, \hat{\mathbf{y}}_{\text{high}}]$ using the inverse CRF function:

$$\hat{\mathbf{p}}_i = \mathcal{R}^{-1}(\hat{\mathbf{y}}_i) \quad i \in \{\text{low}, \text{mid}, \text{high}\}. \quad (22)$$

Finally, the output weights, $[\hat{\mathbf{w}}_{\text{low}}, \hat{\mathbf{w}}_{\text{mid}}, \hat{\mathbf{w}}_{\text{high}}]$, are used to combine coarsely refined cubes $[\hat{\mathbf{p}}_{\text{low}}, \hat{\mathbf{p}}_{\text{mid}}, \hat{\mathbf{p}}_{\text{high}}]$ to form a single HDR video $\hat{\mathbf{p}} \in \mathbb{R}^{N_r \times N_c \times N_t}$:

$$\hat{\mathbf{p}} = \frac{\hat{\mathbf{w}}_{\text{low}} \odot \hat{\mathbf{p}}_{\text{low}} + \hat{\mathbf{w}}_{\text{mid}} \odot \hat{\mathbf{p}}_{\text{mid}} + \hat{\mathbf{w}}_{\text{high}} \odot \hat{\mathbf{p}}_{\text{high}}}{\sum_i \hat{\mathbf{w}}_i}. \quad (23)$$

We adopt the differentiable μ -law function [4], [5] tone-map the training input/output videos, before computing the loss function. To do this, we set the medium exposure $4\mathbf{p}$ as the reference ground truth. Then the estimated tone-mapped video $\hat{\mathbf{I}}$ and ground truth \mathbf{I} are:

$$\hat{\mathbf{I}} = \frac{\log(1 + \mu\hat{\mathbf{p}})}{\log(1 + \mu)}, \quad \mathbf{I} = \frac{\log(1 + 4\mu\mathbf{p})}{\log(1 + \mu)}, \quad (24)$$

where μ is typically set as 5000. Then we minimize the loss function $\mathcal{L}(\cdot)$, described in Section V(B), to fuse HDR frames:

$$\arg \min_{\mathcal{D}_{\text{HDR}}} \mathcal{L}(\hat{\mathbf{I}}, \mathbf{I}). \quad (25)$$

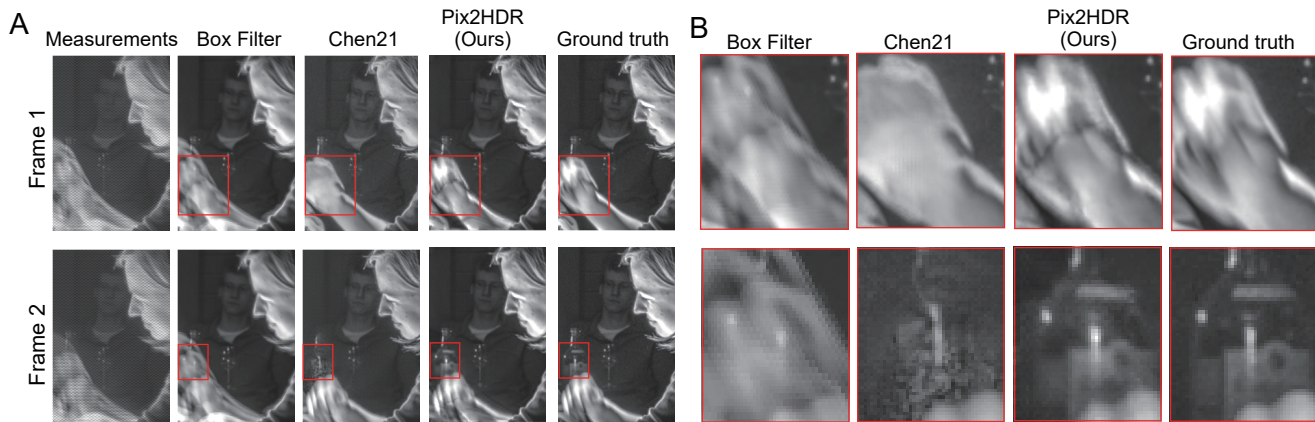


Fig. 9. Example of Pix2HDR and existing methods at resolving HDR videos. **A**. Full frame comparison, **B**. Zoomed in at the motion.

TABLE I
COMPARATIVE METRICS OF PIX2HDR WITH EXISTING METHODS AT RESOLVING HDR VIDEOS

	Sampling method	Synthesis method	PSNR(dB)	SSIM	HDR-VDP	HDR-VQM
Box filter [7]	Spatially varying exposure	Spatial box filter	32.99	0.9679	95.38	50.86
Chen21 [5]	Long-short exposure	2D CNN + Flow net	40.20	0.9364	95.03	54.13
Pix2HDR (ours)	MPVE	3D CNN	43.17	0.9825	95.60	69.90

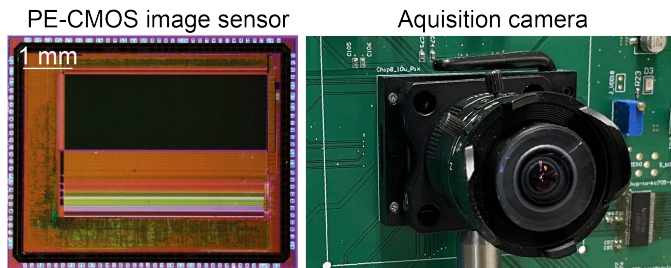


Fig. 10. PE-CMOS image sensor and the acquisition camera.

VI. RESULTS

A. Comparison with previous work using HDR database

We compared the performance of the Pix2HDR method with previous works using the hdm-hdr-2014 dataset [30]. To prepare the training data for the LDR-HDR networks, we first downsample the ground truth video from its resolution (1920×1080) by half to ensure each 128×128 pixel patch has FOV comparable to our camera. We then crop the consecutive frames into $128 \times 128 \times 8$ video cubes for training. The cubes have a 50% overlap along the temporal axis. The training dataset is also augmented with 90° , 180° , and 270° rotated versions. 21 HDR videos are used as training data from the dataset, with one (named Poker Fullshot) used for testing. LDR-net and HDR-net training was completed on a Nvidia RTX3080, and the average inference time to generate one frame is 2.5ms, which supports 400Hz real-time HDR video streaming.

We compare our Pix2HDR method with two prior works: (1) long-short exposure sampling with deep learning synthesis (“Chen21” [5]), (2) and the spatial box filtering [7] (**Fig. 9** and **Table I**). In addition to PSNR and SSIM, we also

measured two addition metrics HDR-VDP [42] and HDR-VQM [43]. HDR-VDP measures normalized differences in physical luminance level between image pairs at different spatial frequency and orientation sub-bands. The differences are pooled into a single score. HDR-VQM also measures luminance differences at various frequency and orientation sub-bands, but error pooling is achieved by spatiotemporal processing, so that the interframe correlations are valued in the video. In both cases, higher scores mean smaller errors.

The Pix2HDR achieves the best performance at all metrics (**Table I**) due to its superior performance at sampling and synthesis. Although both Chen21 and Pix2HDR utilize deep networks for video synthesis, the approaches use different sampling techniques. Chen21 uses interleaved frames at short and long exposure. The long-short exposures inevitably introduce aliasing and blurring when sampling fast motion. This creates considerable difficulty for the CNN and optical flow estimation (flow-net) to recover motions and resolve occlusions during video synthesis. As a result, the quick hand motion in frame 1 is blurred in Chen21, and the occluded bottle label is poorly reconstructed in frame 2 (**Fig. 9B**). On the other hand, Pix2HDR uses the MPVE pixel-wise sampling pattern, which is aliasing-free, with minimized blurring, and robust to occlusion. This yields much better video synthesis results as evident in **Fig. 9**, as well as higher scores in all the metrics (e.g. a boost of 3dB in PSNR).

The Pix2HDR’s LDR-HDR net’s superior synthesis performance is evident when it is compared with the spatial filtering method. Both methods acquired pixel-wise outputs using MPVE sampling but synthesized HDR videos with different techniques. The spatial box filter processes each frame independently without considering its temporal correlations with adjacent frames. The reconstructed video sequence thus suffers from blurring from long exposure pixels. In addition,

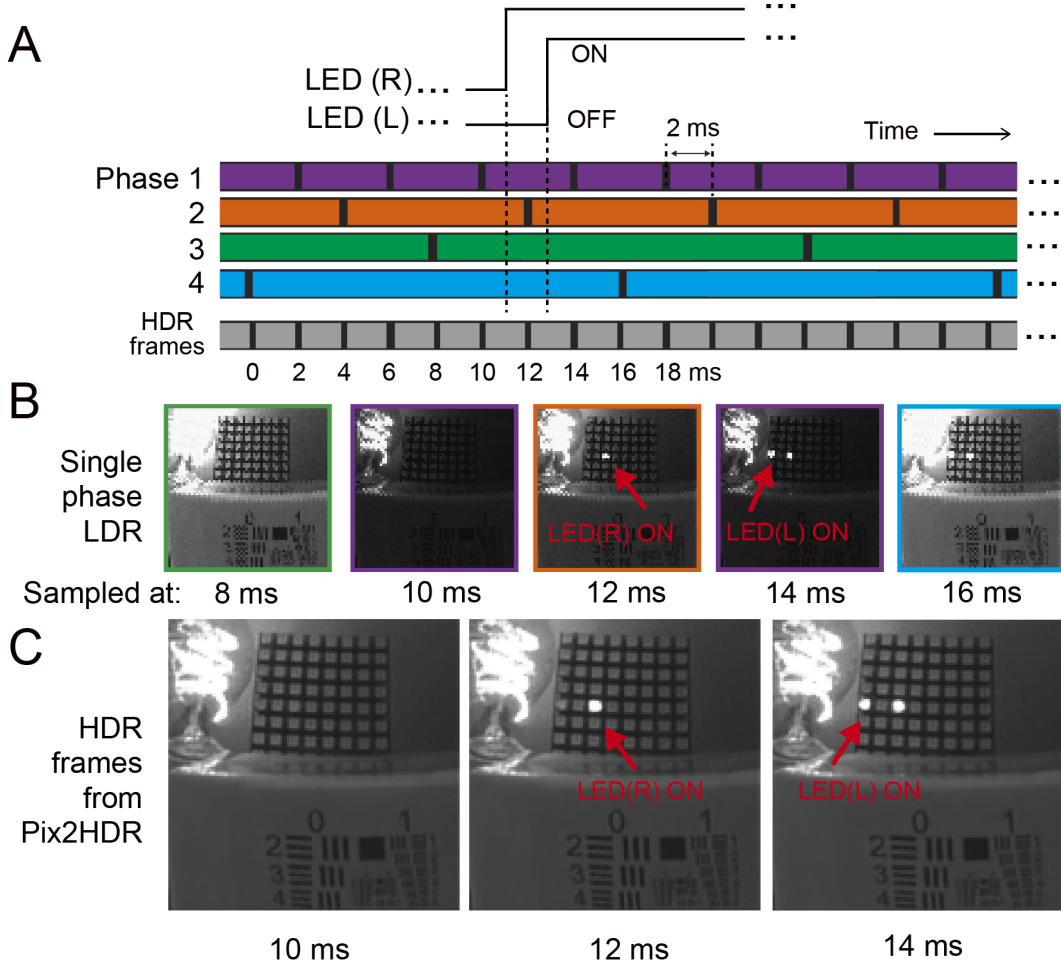


Fig. 11. Capturing transient events faster than individual pixels’ speed in an HDR setting. **A.** Experiment setup: two LEDs (R and L) are switched on sequentially with ~ 2 ms delay. PE-CMOS pixels are configured with 4 ms, 8 ms and 16 ms exposure time. Pixel-wise phase-offset is set to 2 ms and HDR frames are also reconstructed at 2 ms temporal resolution. **B.** Single phase LDR frames. Each individual pixel’s speed (≥ 4 ms sampling period) is insufficient to capture events that are spaced ~ 2 ms in time. But this high-speed event is captured by the phase-offset pixels, achieving temporal resolution of 2 ms. **C.** HDR frames by Pix2HDR portrays the high-speed event with 2 ms temporal resolution.

each frame has a lower resolution due to the low-pass nature of the filter. In contrast, Pix2HDR utilizes LDR-HDR networks to convert pixel-wise outputs directly to high-resolution HDR video cubes, using learned weights that minimize blurring, resulting in notably enhanced performance in all the metrics (**Table I**).

B. Pix2HDR performance at capturing HDR scenes

Next, we assess the Pix2HDR’s performance at capturing real-world HDR scenes. Specifically, we evaluate its temporal resolutions, dynamic range, motion deblurring, and ability to detect object motion under low-light conditions and against bright backgrounds — essential metrics for high-speed HDR imaging.

We build a custom camera using the PE-CMOS image sensor that implements the MPVE pixel-wise sampling pattern (**Fig. 10**). This camera uses a Kintex-7 FPGA to buffer the PE-CMOS sensor’s output and transfers them to a host PC through a high-speed PCIe bus. We implemented the

acquisition software on the PC using the Open-Ephys ONIX API [44], designed for high-speed PCIe interfaces.

1) Temporal Resolution: We first evaluate the Pix2HDR’s temporal resolution at sampling high-speed events. We direct the camera at an LED array, where sequential activation of two LEDs (R and L) takes place with a short time delay (**Fig. 11A**). Our objective is to demonstrate Pix2HDR’s capability to detect the transient ‘ON’ events with time resolution surpassing the camera’s shortest exposure time.

We set up the MPVE with pixel exposures of 4 ms (short), 8 ms (medium), and 16 ms (long). These pixels are organized into four phases, with a minimal phase offset of 2 ms between adjacent pixels (**Fig. 11A**). The LED activation time delay is configured to ~ 2 ms — much faster than the shortest pixel exposure time.

As expected, even the pixels with the shortest exposure time fail to discern the individual LED’s activation events: pixels at phase 1, sampled at 10 ms and 14 ms, do not capture LED R’s activation. This event, however, is unambiguously isolated by pixels with phase offsets at phase 2, sampled at 12

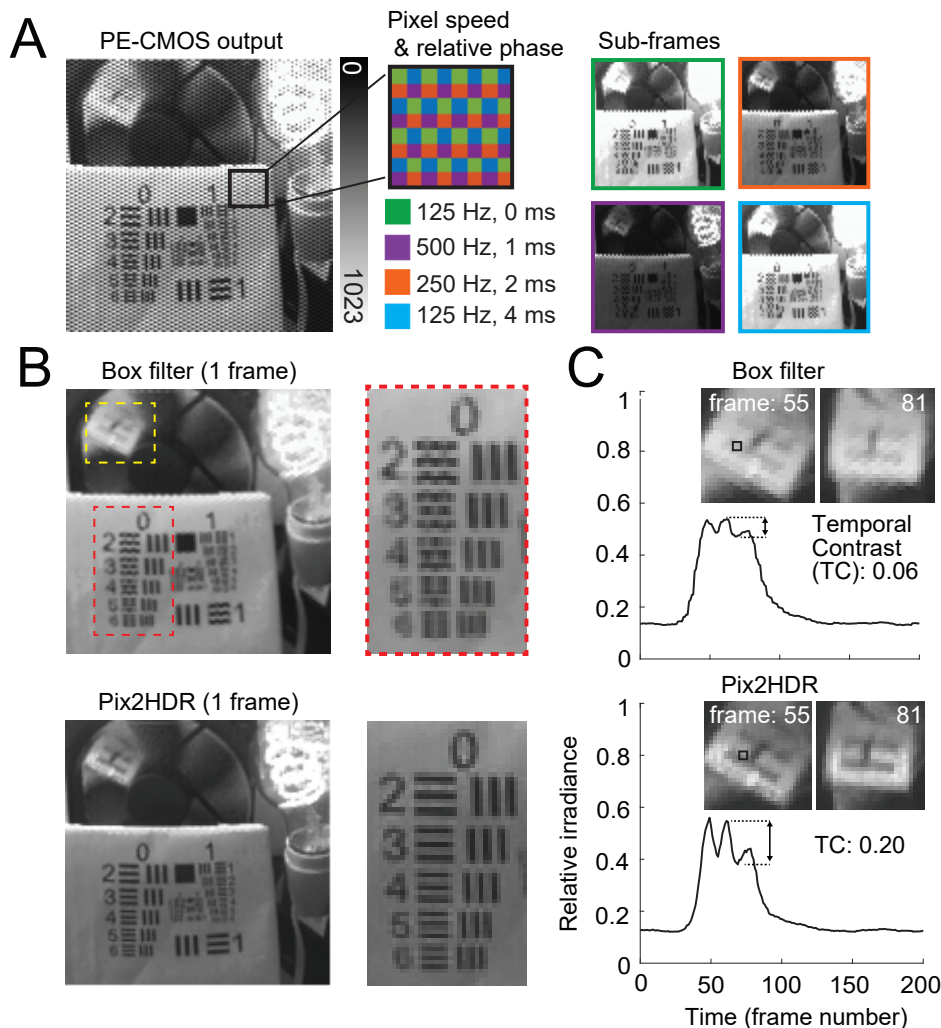


Fig. 12. Capturing HDR video with Pix2HDR. **A**. Direct measurement from PE-CMOS. In any 2×2 pixel patch, pixels are sampling at 2 - 8 ms exposure with 125 - 500 Hz sampling rate, and relative phase shifts of 0 - 4 ms. **B**. Recovered HDR frames (using box filter and Pix2HDR method). The frame from our Pix2HDR has higher spatial contrast and lower blurring to resolve to moving letter “H” with sharper resolution. **C**. Temporal resolution measurements. We fix a single pixel and record its irradiance value across frames. Our Pix2HDR method shows larger irradiance variation corresponding to the motion of the “H” and thereby results in a much higher temporal contrast (TC = 0.2) than box filter (TC = 0.06).

ms (**Fig. 11B**). Between phase-shifted pixels, Pix2HDR can resolve a temporal resolution of 2 ms (500 Hz), two times faster than the shorted pixels exposure at 4 ms (250 Hz). Consequently, Pix2HDR can synthesize HDR video sequences at a time resolution of 2 ms with 500 FPS (**Fig. 11C**).

2) *Dynamic range and deblurring performance*: Next, we assess the Pix2HDR’s performance at capturing motion in an HDR context. We set up a scene with diverse intensity and motions: a bright area created by a light bulb, a dark region with a USAF target, and a fan rotating at a speed of ~ 300 rpm, with a letter “H” printed on it. To capture this scene, we configured the MPVE with pixel exposures of 2 ms (short), 4 ms (medium), and 8 ms (long), with a 1 ms minimal pixel-wise phase offset (**Fig. 12A**). Pixels raw outputs are displayed by grouping into subframe with 1/4 spatial resolution. Short exposure pixels capture blurred free motion and avoid overexposure at the bright region at the cost of lower SNR. Pixels with longer exposures enhance the SNR

at the expense of blurring and overexposure.

We combined the pixel-wise outputs to form an HDR video sequence with the LDR-HDR nets and then compared the synthesized sequences with those constructed through a spatial box filter. The Pix2HDR results have better HDR spatial contrast and resolution, notably in the reconstructed light blub and the USAF target (**Fig. 12B**). To quantify the motion trajectory, we take the intensity of a single pixel located along the path of the rotation motion. As the letter “H” passes through it, it generates a time-varying intensity, v , corresponding to the letter’s strokes’ trajectory (**Fig. 12C**). We slightly modified the Michelson contrast [45] to temporal axis and calculated the temporal contrast (TC) of v , during a pass-through event:

$$TC = \frac{v_{\text{peak}} - v_{\text{through}}}{v_{\text{peak}} + v_{\text{through}}}. \quad (26)$$

The TC quantifies the overall detectability of a motion pattern. It is affected by a few spatial and temporal factors:

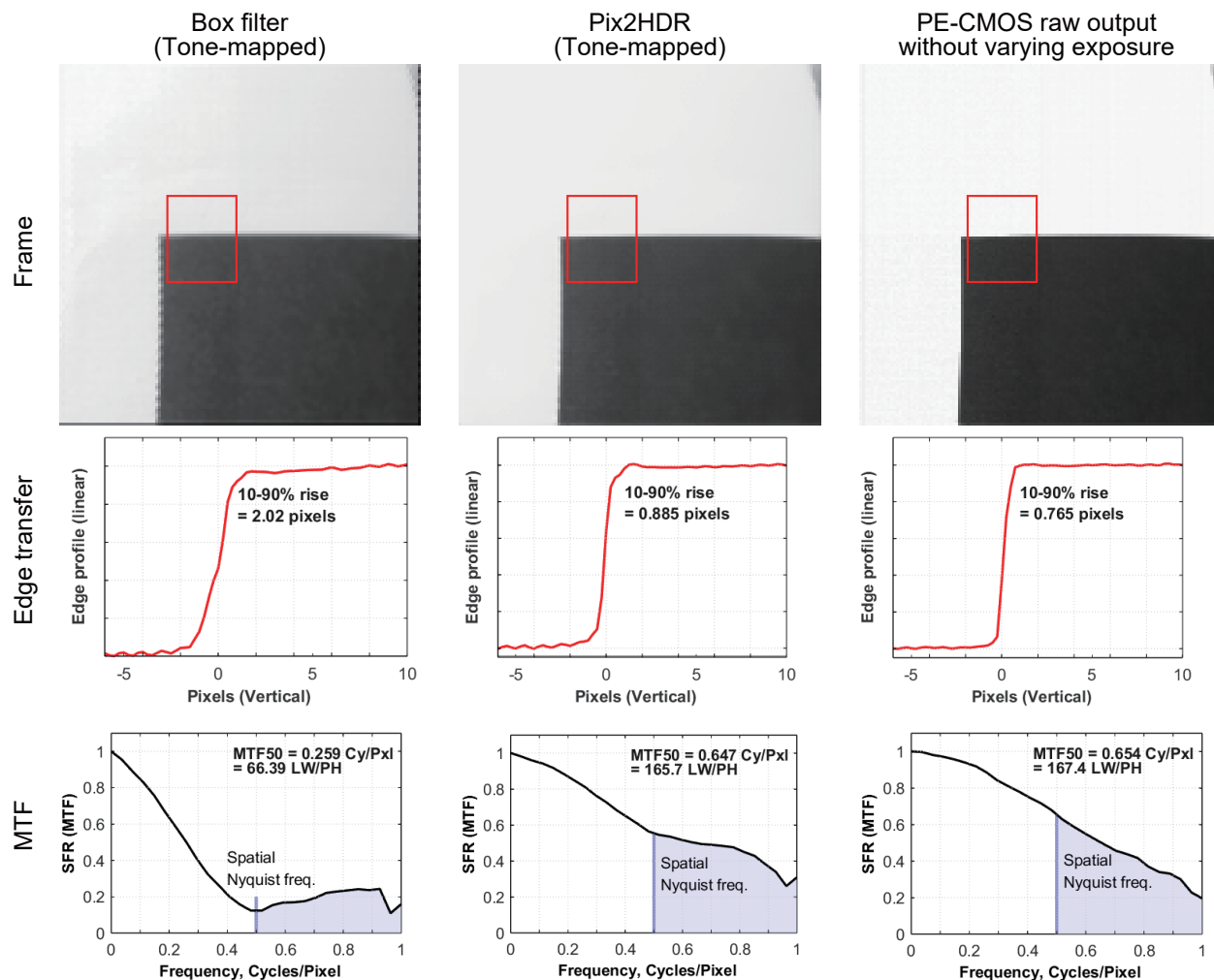


Fig. 13. Comparison of edge transfers and MTFs among HDR frames (from box filter and Pix2HDR) and direct LDR output from PE-CMOS. To qualify the spatial resolution, we measure the edge transfers and MTFs in a region with abrupt transition from dark to bright. Compared with the raw output from PE-CMOS, the frame from our Pix2HDR only has tiny distance prolongation in 10-90% rise rate and little drop in MTF50 value, which means our Pix2HDR method only loses neglectable spatial resolution after reconstruction. Meanwhile, the box filter gives much worse scores in the metrics and even generates jagged vertical edge in the recovered frame.

SNR, spatial contrast, and motion blurring, as smoothed edges can lead to TC value degradation. Pix2HDR’s synthesized HDR frames exhibit significantly improved TC compared to box-filtered outputs, clearly resolving the edges of the fast-moving letter “H” (Fig. 12C).

3) *Spatial resolution*: To quantify Pix2HDR’s spatial resolution, we measured its modulation transfer functions (MTFs) using the slanted-edge method [46]. The target scene contains a single edge that abruptly transitions from dark to bright. We then synthesized the HDR frames from MPVE pixel-wise outputs with the Pix2HDR and box filtering.

The edge transfer and MTF all indicate higher spatial resolution for Pix2HDR at preserving sharp edges (Fig. 13). MTF50 denotes the spatial frequency where contrast drops to 50% of its original value — a higher MTF50 score signifies a sharper, more detailed image. As the recovery strategies (box filter and Pix2HDR) inevitably cause sharpness loss in above frames, we also acquired the full-resolution frame using PE-CMOS with fixed pixel-wise exposures and set its scores as the theoretical

limits to the camera optics and pixel pitch. Pix2HDR achieves superior edge transfer (0.885 pixels for 10-90% rise rate) and MTF50 values (0.647 cycles/pixel), surpassing those from the box-filtered output and approaching theoretical limits of 0.765 pixels and 0.654 cycles/pixel, respectively.

4) *Motion detection under low-light conditions*: We then showcase that Pix2HDR can harness the benefits of short and long pixel exposures to track movement, particularly for detecting fast motion in low-light conditions - a challenging task for video acquisition. We dim the ambient light for the demonstration and set a fan with the “H” logo printed on it into a rotational motion (Fig. 14A-D). This creates a low-light condition for resolving motion in the dark. We sampled the scene with the MPVE using exposures of 2 ms (short), 4 ms (medium), and 8 ms (long), with a 1 ms minimal pixel-wise phase offset.

For metrics, in addition to TC, we also calculate the motion trajectory’s full duration (FD) to quantify blurring. We define FD as the timespan between 15% of the peak irradiance

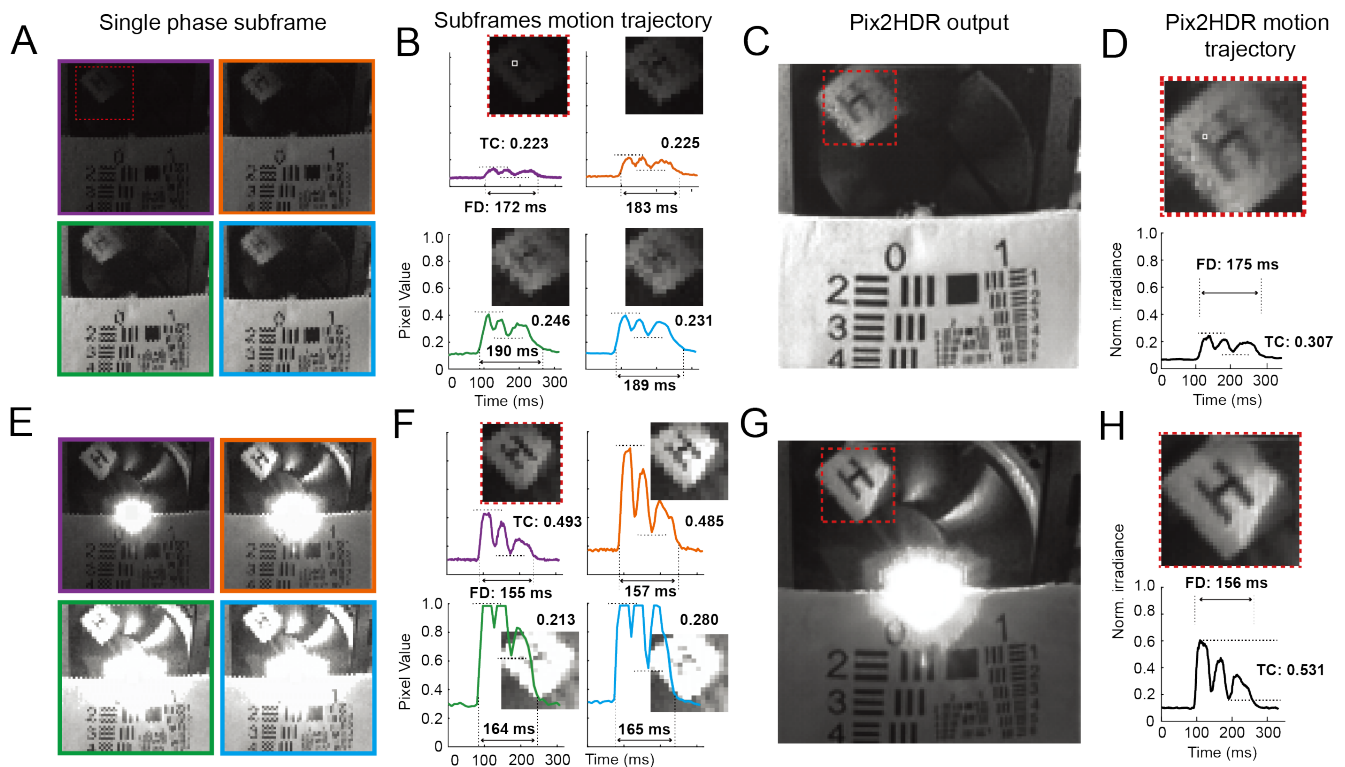


Fig. 14. Imaging fast motion in dark and against bright background. **A.** Subframes of PE-CMOS outputs under low illumination conditions. **B.** Time series of a single pixel value indicating the advantage of different exposures at capturing motion: Long exposure subframes have higher temporal contrast (TC) at resolving the motion of the letter “H”, while short exposure subframes have the shortest full duration (FD), indicating minimal blurring. **C-D.** Pix2HDR output (**C**, single frame, and **D**, pixel time-series). Pix2HDR combines the strength of long and short exposures, resulting in the highest TC compared. Its FD is close to that of short exposure subframes, indicating superior performance at resolving motion in the dark. **E-H.** Pix2HDR at resolving motion against the bright background. Its high TC and low FD indicates Pix2HDR’s robust performance in resolving motion amid overexposures.

measured from the rising and falling edges (**Fig. 14B**). The shorter the FD, the less the blurring in the motion trajectory.

In low ambient light conditions, pixels at different exposures have distinct advantages in terms of temporal contrast or motion blurring. Long exposures pixels show the highest temporal contrast (TC: 0.246) in comparison to those undergoing medium and short exposures (0.223) (**Fig. 14B**). Meanwhile, short exposures have the minimum amount of motion blurring (FD: 172 ms), compared with medium and long exposures at 183 - 190 ms. Both the TC and FD are pure temporal metrics derived from a single pixel. They effectively resemble the outcome if cameras with the same exposures were employed.

From the subframes, the Pix2HDR’s LDR-HDR net synthesizes a high-resolution video from pixel-wise outputs, resulting in enhanced temporal contrast (TC: 0.307) while simultaneously maintaining minimal blurring (FD: 175 ms). This highlights the Pix2HDR’s advantage over single-exposure cameras in tracking motion trajectories in low light conditions.

5) *Motion detection with bright background:* Last, we demonstrate the PixHDR’s ability to resolve motion against a bright background to evaluate its ability to capture fast movement amid overexposures. Using the same setup, we turned on a bright LED light in the middle of the FOV (**Fig.14 E-H**). The bright light produces various degrees of blooming effects at each subframes.

While the additional light improved the temporal contrast

of short and medium exposure (TC: 0.493 and 0.485), the blooming effects caused large overexposures in subframes with long exposures. The clipping of pixel values leads to long-exposure subframes having low temporal contrast (TC: 0.213 and 0.280). Pix2HDR’s synthesized HDR videos are robust against overexposures. The temporal contrast value is even enhanced (TC: 0.531) while the full duration (FD: 156 ms) is kept short, indicating minimal motion blurring.

These benchtop demos in this section seek to mimic challenging conditions encountered during real-world vision applications, such as motion capture at night and against a bright headlight of incoming vehicles. The results of the demonstration showed the advantages of Pix2HDR at capturing motion during extreme conditions of low light and against bright background, having better motion detection performance than conventional cameras with fixed pixel exposures.

VII. DISCUSSION

We have demonstrated that by combining a versatile pixel-wise sampling method with the strength of the neural networks in decoding complex light and motion patterns, Pix2HDR significantly outperforms existing methods in capturing motion in HDR settings. This makes Pix2HDR as an ideal solution for motion-tracking applications in robotics, AR/VR, and autonomous vehicles, among other vision applications. Our sensor is also compact and power-efficient. The pixel-wise

sampling is implemented using the pixel circuitry and it achieves high temporal resolution using low data rate. The sensor These features feature makes Pix2HDR applicable for mobile applications

In future developments, several aspects of Pix2HDR can be further improved. On the sampling side, although the MPVE sampling pattern is well-optimized for general use, there are opportunities to tailor pixel-wise sampling to specific applications to enhance dynamic range or elevate temporal resolution. The sampling pattern can also be integrated into a closed-loop system, allowing it to adapt dynamically to changing scenes [14]. On the synthesis side, the training steps can be made more generalizable. Currently, when creating the training dataset, camera-specific CRFs are used to map ground truth videos to each camera's output. This specificity ties the trained network weights to individual cameras. A more generalized approach could involve training the network with an overall gamma correction and mapping the captured frames from each camera to a pre-defined transfer function before network migration.

The Pix2HDR approach aligns with the general trend of image sensor technology development. With advancements in CMOS technology, which enable the reduction of transistor size and allow 3D integration of the pixel array and processing chips, the next generation of image sensor development is emphasizing pixel-level reconfigurability with edge processing. By combining versatile pixel-wise sampling with learning-based HDR synthesis methods that can be implemented at the edge, Pix2HDR enhances the adaptability of vision systems in dynamic conditions, addressing the growing demands of vision applications.

REFERENCES

- [1] B. Wilburn, N. Joshi, V. Vaish, E.-V. Talvala, E. Antunez, A. Barth, A. Adams, M. Horowitz, and M. Levoy, "High performance imaging using large camera arrays," in *ACM SIGGRAPH 2005 Papers*, 2005, pp. 765–776.
- [2] V. Popovic, K. Seyid, E. Pignat, Ö. Çoğal, and Y. Leblebici, "Multi-camera platform for panoramic real-time hdr video construction and rendering," *Journal of Real-Time Image Processing*, vol. 12, pp. 697–708, 2016.
- [3] M. D. Tocci, C. Kiser, N. Tocci, and P. Sen, "A versatile hdr video production system," *ACM Transactions on Graphics (TOG)*, vol. 30, no. 4, pp. 1–10, 2011.
- [4] N. K. Kalantari and R. Ramamoorthi, "Deep hdr video from sequences with alternating exposures," in *Computer graphics forum*, vol. 38, no. 2. Wiley Online Library, 2019, pp. 193–205.
- [5] G. Chen, C. Chen, S. Guo, Z. Liang, K.-Y. K. Wong, and L. Zhang, "Hdr video reconstruction: A coarse-to-fine network and a real-world benchmark dataset," in *Proceedings of the IEEE/CVF International Conference on Computer Vision*, 2021, pp. 2502–2511.
- [6] J. N. Martel, L. K. Mueller, S. J. Carey, P. Dudek, and G. Wetzstein, "Neural sensors: Learning pixel exposures for hdr imaging and video compressive sensing with programmable sensors," *IEEE transactions on pattern analysis and machine intelligence*, vol. 42, no. 7, pp. 1642–1653, 2020.
- [7] S. K. Nayar and T. Mitsunaga, "High dynamic range imaging: Spatially varying pixel exposures," in *Proceedings IEEE Conference on Computer Vision and Pattern Recognition. CVPR 2000 (Cat. No. PR00662)*, vol. 1. IEEE, 2000, pp. 472–479.
- [8] S. K. Nayar, V. Branzoi, and T. E. Boult, "Programmable imaging: Towards a flexible camera," *International Journal of Computer Vision*, vol. 70, pp. 7–22, 2006.
- [9] A. Serrano, F. Heide, D. Gutierrez, G. Wetzstein, and B. Masia, "Convolutional sparse coding for high dynamic range imaging," in *Computer Graphics Forum*, vol. 35, no. 2. Wiley Online Library, 2016, pp. 153–163.
- [10] M. M. Alghamdi, Q. Fu, A. K. Thabet, and W. Heidrich, "Reconfigurable snapshot hdr imaging using coded masks and inception network," 2019.
- [11] R. Gulve, N. Sarhangnejad, G. Dutta, M. Sakr, D. Nguyen, R. Rangel, W. Chen, Z. Xia, M. Wei, N. Gusev *et al.*, "39 000-subexposures/s dual-adc cmos image sensor with dual-tap coded-exposure pixels for single-shot hdr and 3-d computational imaging," *IEEE Journal of Solid-State Circuits*, 2023.
- [12] Y. Luo and S. Mirabbasi, "A 30-fps 192× 192 cmos image sensor with per-frame spatial-temporal coded exposure for compressive focal-stack depth sensing," *IEEE Journal of Solid-State Circuits*, vol. 57, no. 6, pp. 1661–1672, 2022.
- [13] S. Hajisharif, J. Kronander, and J. Unger, "Adaptive dualiso hdr reconstruction," *EURASIP Journal on Image and Video Processing*, vol. 2015, no. 1, pp. 1–13, 2015.
- [14] J. Zhang, J. P. Newman, X. Wang, C. S. Thakur, J. Rattray, R. Etienne-Cummings, and M. A. Wilson, "A closed-loop, all-electronic pixel-wise adaptive imaging system for high dynamic range videography," *IEEE Transactions on Circuits and Systems I: Regular Papers*, vol. 67, no. 6, pp. 1803–1814, 2020.
- [15] J. Zhang, T. Xiong, T. Tran, S. Chin, and R. Etienne-Cummings, "Compact all-cmos spatiotemporal compressive sensing video camera with pixel-wise coded exposure," *Optics express*, vol. 24, no. 8, pp. 9013–9024, 2016.
- [16] T. Portz, L. Zhang, and H. Jiang, "Random coded sampling for high-speed hdr video," in *IEEE International Conference on Computational Photography (ICCP)*. IEEE, 2013, pp. 1–8.
- [17] T. Mitsunaga and S. K. Nayar, "Radiometric self calibration," in *Proceedings. 1999 IEEE computer society conference on computer vision and pattern recognition (Cat. No PR00149)*, vol. 1. IEEE, 1999, pp. 374–380.
- [18] P. E. Debevec and J. Malik, "Recovering high dynamic range radiance maps from photographs," in *Seminal Graphics Papers: Pushing the Boundaries, Volume 2*, 2023, pp. 643–652.
- [19] E. Reinhard, W. Heidrich, P. Debevec, S. Pattanaik, G. Ward, and K. Myszkowski, *High dynamic range imaging: acquisition, display, and image-based lighting*. Morgan Kaufmann, 2010.
- [20] O. Gallo, N. Gelfandz, W.-C. Chen, M. Tico, and K. Pulli, "Artifact-free high dynamic range imaging," in *2009 IEEE International conference on computational photography (ICCP)*. IEEE, 2009, pp. 1–7.
- [21] P. Sen, N. K. Kalantari, M. Yaesoubi, S. Darabi, D. B. Goldman, and E. Shechtman, "Robust patch-based hdr reconstruction of dynamic scenes," *ACM Trans. Graph.*, vol. 31, no. 6, pp. 203–1, 2012.
- [22] T.-H. Oh, J.-Y. Lee, Y.-W. Tai, and I. S. Kweon, "Robust high dynamic range imaging by rank minimization," *IEEE transactions on pattern analysis and machine intelligence*, vol. 37, no. 6, pp. 1219–1232, 2014.
- [23] N. K. Kalantari, R. Ramamoorthi *et al.*, "Deep high dynamic range imaging of dynamic scenes," *ACM Trans. Graph.*, vol. 36, no. 4, pp. 144–1, 2017.
- [24] J. Cai, S. Gu, and L. Zhang, "Learning a deep single image contrast enhancer from multi-exposure images," *IEEE Transactions on Image Processing*, vol. 27, no. 4, pp. 2049–2062, 2018.
- [25] Q. Yan, L. Zhang, Y. Liu, Y. Zhu, J. Sun, Q. Shi, and Y. Zhang, "Deep hdr imaging via a non-local network," *IEEE Transactions on Image Processing*, vol. 29, pp. 4308–4322, 2020.
- [26] S. Yao, "Robust image registration for multiple exposure high dynamic range image synthesis," in *Image Processing: Algorithms and Systems IX*, vol. 7870. SPIE, 2011, pp. 216–224.
- [27] S. Baker, D. Scharstein, J. Lewis, S. Roth, M. J. Black, and R. Szeliski, "A database and evaluation methodology for optical flow," *International journal of computer vision*, vol. 92, pp. 1–31, 2011.
- [28] H. Zimmer, A. Bruhn, and J. Weickert, "Freehand hdr imaging of moving scenes with simultaneous resolution enhancement," in *Computer Graphics Forum*, vol. 30, no. 2. Wiley Online Library, 2011, pp. 405–414.
- [29] M. McGuire, W. Matusik, H. Pfister, B. Chen, J. F. Hughes, and S. K. Nayar, "Optical splitting trees for high-precision monocular imaging," *IEEE Computer Graphics and Applications*, vol. 27, no. 2, pp. 32–42, 2007.
- [30] J. Froehlich, S. Grandinetti, B. Eberhardt, S. Walter, A. Schilling, and H. Brendel, "Creating cinematic wide gamut hdr-video for the evaluation of tone mapping operators and hdr-displays," in *Digital photography X*, vol. 9023. SPIE, 2014, pp. 279–288.

- [31] V. Ramachandra, M. Zwicker, and T. Nguyen, "Hdr imaging from differently exposed multiview videos," in *2008 3DTV Conference: The True Vision-Capture, Transmission and Display of 3D Video*. IEEE, 2008, pp. 85–88.
- [32] Nayar and Branzoi, "Adaptive dynamic range imaging: Optical control of pixel exposures over space and time," in *Proceedings Ninth IEEE International Conference on Computer Vision*. IEEE, 2003, pp. 1168–1175.
- [33] S. J. Carey, A. Lopich, D. R. Barr, B. Wang, and P. Dudek, "A 100,000 fps vision sensor with embedded 535gops/w 256× 256 simd processor array," in *2013 symposium on VLSI circuits*. IEEE, 2013, pp. C182–C183.
- [34] Y. Jiang, I. Choi, J. Jiang, and J. Gu, "Hdr video reconstruction with tri-exposure quad-bayer sensors," *arXiv preprint arXiv:2103.10982*, 2021.
- [35] U. Cogalan, M. Bemana, K. Myszkowski, H.-P. Seidel, and T. Ritschel, "Learning hdr video reconstruction for dual-exposure sensors with temporally-alternating exposures," *Computers & Graphics*, vol. 105, pp. 57–72, 2022.
- [36] J. Zhang, J. Newman, Z. Wang, Y. Qian, W. Guo, Z. S. Chen, C. Linghu, R. Etienne-Cummings, E. Fossum, E. Boyden *et al.*, "Pixel-wise programmability enables dynamic high-snr cameras for high-speed microscopy," *bioRxiv*, pp. 2023–06, 2023.
- [37] A. Agrawal, Y. Xu, and R. Raskar, "Invertible motion blur in video," in *ACM SIGGRAPH 2009 papers*, 2009, pp. 1–8.
- [38] D. P. Kingma and J. Ba, "Adam: A method for stochastic optimization," *arXiv preprint arXiv:1412.6980*, 2014.
- [39] K. Simonyan and A. Zisserman, "Very deep convolutional networks for large-scale image recognition," *arXiv preprint arXiv:1409.1556*, 2014.
- [40] J. Snell, K. Ridgeway, R. Liao, B. D. Roads, M. C. Mozer, and R. S. Zemel, "Learning to generate images with perceptual similarity metrics," in *2017 IEEE International Conference on Image Processing (ICIP)*. IEEE, 2017, pp. 4277–4281.
- [41] H. Zhao, O. Gallo, I. Frosio, and J. Kautz, "Loss functions for image restoration with neural networks," *IEEE Transactions on computational imaging*, vol. 3, no. 1, pp. 47–57, 2016.
- [42] R. Mantiuk, K. J. Kim, A. G. Rempel, and W. Heidrich, "Hdr-vdp-2: A calibrated visual metric for visibility and quality predictions in all luminance conditions," *ACM Transactions on graphics (TOG)*, vol. 30, no. 4, pp. 1–14, 2011.
- [43] M. Narwaria, M. P. Da Silva, and P. Le Callet, "Hdr-vqm: An objective quality measure for high dynamic range video," *Signal Processing: Image Communication*, vol. 35, pp. 46–60, 2015.
- [44] J. P. Newman, J. Zhang, A. Cuevas-Lopez, N. J. Miller, T. Honda, M.-S. H. van der Goes, A. H. Leighton, F. Carvalho, G. Lopes, A. Lakunina *et al.*, "A unified open-source platform for multimodal neural recording and perturbation during naturalistic behavior," *bioRxiv*, pp. 2023–08, 2023.
- [45] E. Peli, "Contrast in complex images," *JOSA A*, vol. 7, no. 10, pp. 2032–2040, 1990.
- [46] M. Estrieau and P. Magnan, "Fast mtf measurement of cmos imagers using iso 12333 slanted-edge methodology," in *Detectors and Associated Signal Processing*, vol. 5251. SPIE, 2004, pp. 243–252.